HHS Public Access

Author manuscript

IEEE Sens J. Author manuscript; available in PMC 2017 December 01.

Published in final edited form as:

IEEE Sens J. 2016 December 1; 16(23): 8381–8388. doi:10.1109/JSEN.2016.2611569.

Non-Contact Photoacoustic Imaging Using a Commercial Heterodyne Interferometer

Chao Tian [Member, IEEE],
Department of Biomedical Engineering, University of Michigan, Ann Arbor, MI 48109 USA

Ting Feng,
Department of Electronic Science and Engineering, Nanjing University, Nanjing 21000, China, and also with the Department of Radiology, University of Michigan, Ann Arbor, MI 48109 USA

Cheng Wang,
School of Medical Instrument and Food Engineering, University of Shanghai for Science and Technology, Shanghai 200093, China

Shengchun Liu,
College of Physical Science and Technology, Heilongjiang University, Harbin 150080, China

Qian Cheng,
Institute of Acoustics, Tongji University, Shanghai 200092, China

David E. Oliver,
Polytec, Inc., Irvine, CA 92618 USA

Xueding Wang, and
Department of Biomedical Engineering and the Department of Radiology, University of Michigan, Ann Arbor, MI 48109 USA, and also with the Institute of Acoustics, Tongji University, Shanghai 200092, China

Guan Xu
Department of Radiology, University of Michigan, Ann Arbor, MI 48109 USA

Abstract

Most current photoacoustic imaging (PAI) systems employ piezoelectric transducers to receive photoacoustic signals, which requires coupling medium to facilitate photoacoustic wave propagation and are not favored in many applications. Here, we report an all-optical non-contact PAI system based on a commercial heterodyne interferometer working at 1550 nm. The interferometer remotely detects ultrasound-induced surface vibration and does not involve any physical contact with the sample. The theoretically predicated and experimentally measured noise equivalent detection limits of the optical sensor are about 4.5 and 810 Pa over 1.2 MHz bandwidth. Using a raster-scan PAI system equipped with the non-contact design, stereotactic boundaries of an artificial tumor in a pig brain were accurately delineated. The non-contact design also enables the tomographic PAI of biological tissue samples in a non-invasive manner. The preliminary

Correspondence to: Guan Xu.

results and analyses reveal that the heterodyne interferometer-based non-contact PAI system holds good potential in biomedical imaging.

Index Terms

Biophotonics; photoacoustic imaging; interferometry; remote sensing

I. Introduction

Photoacoustic Imaging (PAI), which combines the merits of the high contrast of optical imaging and the good penetration of ultrasound imaging, is a hybrid and non-invasive imaging modality, and has been extensively explored for various biomedical applications [1]–[7]. A PAI system typically involves two major parts, that is, optical excitation of biological absorbers by pulsed laser and acoustic detection by ultrasonic sensor. Of the two, the latter plays a substantial role in the final imaging results.

Current PAI systems prevailingly employ piezoelectric transducers for PA signal detection [1]–[4], [8], [9]. In spite of their high sensitivity, this type of transducers has several limitations. First, piezoelectric transducer usually has a narrow frequency bandwidth and can only respond to part of the inherently broadband PA signals. The loss of low-and/or high-frequency components limits the imaging spatial resolution [2]. Second, piezoelectric transducer typically has a finite aperture size, which results in degraded imaging quality due to the violation of the point detector assumption required by most reconstruction algorithms [10]. Third, piezoelectric transducers may physically interfere with the excitation laser beam when working in the reflection mode. Moreover, to facilitate PA wave propagation, acoustic coupling medium (such as water or gel) needs to be applied between the transducer and the sample. Although this is not a problem in most situations, being able to image in a completely non-contact manner is highly desirable in specific applications, such as image-guided brain surgery [11], wound assessment [12], and ophthalmology [13]. The practical difficulties have raised much awareness and are stimulating recent developments of novel ultrasound detection methods in PAI.

Optical detection of ultrasound, which has been extensively researched for several decades, could overcome the limitations of conventional piezoelectric transducers and serve as an alternative. To date, various types of optical sensors for ultrasound detection have been developed. These optical sensors could be categorized into two major types, i.e., contact optical sensor and non-contact optical sensor. Contact optical sensor normally uses water or acoustic gel to couple ultrasound from the sample to the sensor [14]–[30]. This type of optical sensor includes the Fabry-Perot polymer film sensor [14]–[20], the micro-ring sensor [21]–[26], the fiber Bragg grating sensor [27], the probe beam deflection based sensor [28], etc. Contact optical sensor usually has comparable sensitivity with conventional piezoelectric transducer, but still needs coupling medium for PA signal reception. The second type, i.e., non-contact optical sensor, can detect PA signal remotely without any physical contact with the sample. It usually utilizes phase- or frequency-modulated light backscattered from sample surface to interferometrically detect ultrasound-induced surface

vibration and can be remotely performed [31]–[39]. Exploratory studies have been focused on heterodyne interferometry [31], optical fiber-based interferometry [32], two-wave mixing interferometry [33], multi-beam Fabry-Perot interferometry [34], [35], low-coherence interferometry [36]–[38], full-field speckle interferometry [39], etc. Due to its advantages, non-contact optical sensing of ultrasound holds substantial promise in PAI.

In this work, we report an all-optical non-contact PAI system based on a commercially available heterodyne interferometer (RSV-150, Polytec, Irvine, CA). The model RSV-150 working at 1550nm was chosen because it has higher sensitivity than shorter-wavelength interferometers [40]. The main purpose of the study is to systematically evaluate the performance of the heterodyne interferometer in PAI from both theory and experiment, and explore the feasibility of non-contact PAI in a non-invasive manner. We will first introduce the principle of the interferometer, then present the findings from performance characterization, and finally show the imaging results obtained on biological samples.

II. Optical Heterodyne Measurement

Figure 1 shows the Mach-Zehnder configuration of the heterodyne interferometer. The emitted laser beam at 1550 nm is split by the beam splitter 1 (BS1) into two components, i.e., the measurement (red) and the reference (blue) beams. The measurement beam, after transmitting through BS2, is focused onto the sample by an objective, phase modulated by ultrasound-induced surface vibration, backscattered into the interferometer, and finally reflected to the photodetector. The reference beam, after being reflected by BS3, experiences a steady frequency shift (e.g., f_B = 40 MHz) induced by an acoustic-optic modulator or Bragg cell, and is reflected by BS4 to the same photodetector. The measurement beam and the reference beam interfere with each other after they meet after BS4, which produces a periodic intensity modulation of the voltage output of the photodetector. The voltage signal is split into two parts, which are mixed with two quadrature signals generated by a local oscillator (LO), low-pass (LP) filtered, and finally computed for instantaneous surface displacement or velocity output. The mathematical formulation is presented below.

Using the representation of plane mechanical wave, ultrasound-induced surface particle displacement δ can be written as

$$\delta(t)=\delta_{\max}\cos(2\pi f_u t), \quad (1)$$

where δ_{max} is the amplitude and f_u is the ultrasonic frequency. Surface particle velocity is the derivative of instantaneous displacement, that is,

$$v(t)=\frac{d\delta(t)}{dt}=-2\pi f_u\delta_{\max}\sin(2\pi f_u t). \quad (2)$$

Using the representation of plane electromagnetic wave, the beam from the laser can be expressed as

$$E=E_0\exp[\mathrm{i}(\omega\mathrm{t}-\mathrm{kz}+\varphi)], \quad (3)$$

where E_0 is the amplitude, $\omega = 2\pi f$ is the angular frequency, f is the laser frequency, $k = 2\pi/\lambda$ is the wave number, φ is the initial phase, and z is the propagation direction of the wave. In this way, the reference beam with a frequency shift f_B induced by the Bragg cell can be written as

$$E_1=E_{10}\exp i[(\omega+\omega_B)t-kz_1+\varphi], \quad (4)$$

where $\omega_B = 2\pi f_B$ and E_{10} is the amplitude. The measurement beam with phase modulation caused by surface particle displacement δ can be written as

$$E_2=E_{20}\exp(i\{\omega t-k[z_2-2\delta(t)]+\varphi\}), \quad (5)$$

where E_{20} is the amplitude. The interference signal on the detector can be obtained as

$$I=|(E_1+E_2)|^2=E_1^2+E_2^2+2E_1E_2\cos[\omega_B t-2k\delta(t)+\phi_0], \quad (6)$$

where the bracket ‖ means the mode, and $\phi_0 = -k(z_1 - z_2)$ is the constant phase difference.

To allow for digital demodulation, the intensity signal I is split and multiplied by two quadrature signals $\cos\omega_B t$ and $\sin\omega_B t$ generated by the LO [Fig. 1(b)], which can be written as

$$I\cdot\cos\omega_B t=(E_1^2+E_2^2)\cos\omega_B t+E_1E_2\cos[2\omega_B t-2k\delta(t)+\phi_0]+E_1E_2\cos[2k\delta(t)-\phi_0], \quad (7)$$

$$I\cdot\sin\omega_B t=(E_1^2+E_2^2)\sin\omega_B t+E_1E_2\sin[2\omega_B t-2k\delta(t)+\phi_0]+E_1E_2\sin[2k\delta(t)-\phi_0]. \quad (8)$$

By low-pass filtering the high-frequency (ω_B and $2\omega_B$) components, the two signals are transformed into the in-phase signal (I signal) and the quadrature signal (Q signal), i.e.,

$$I(t)=E_1E_2\cos[2k\delta(t)-\phi_0], \quad (9)$$

$$Q(t)=E_1E_2\sin[2k\delta(t)-\phi_0]. \quad (10)$$

The instantaneous surface particle displacement δ can be reconstructed as

$$\delta(t)=\frac{\lambda}{4\pi}\left\{\arctan\left[\frac{Q(t)}{I(t)}\right]+\phi_0\right\}. \quad (11)$$

Note that ϕ_0 is a constant. The surface particle velocity υ can be accordingly obtained by finding the derivative of δ [Eq. (2)].

III. Performance Characterization

A phantom experiment was performed to characterize the receiving sensitivity and bandwidth of the interferometer. A phantom [Fig. 2(a)] with a diameter of 25 mm, was made from 10% porcine gel (G2500, Sigma-Aldrich, St. Louis, MO). A 500 μm diameter polyethylene microsphere (BK500T, Thermo Fisher Scientific, Waltham, MA) was placed in the center of the sample as a point target. The phantom was excited by a 532 nm pulsed laser (Powerlite DLS 8010, Continuum Inc., San Jose, CA) at a fluence of about 18 mJ·cm^{-2}. The probe laser beam of the interferometer was perpendicularly pointed at the side surface of the phantom to detect surface vibration caused by generated PA signals. After excitation by the laser pulses, PA signals were initially generated at the optically absorbing microsphere, then propagated to the phantom surface, and were finally detected by the laser interferometer, as a typical signal shown in Fig 2(b).

To quantify the sensitivity and the bandwidth of the interferometer, the measurement was also conducted by using a needle hydrophone (HNC-1500, Onda Co., Sunnyvale, CA) whose frequency response from 0.1 MHz to 10 MHz had been calibrated. In the experiment, the active tip of the needle hydrophone gently touched the side surface of the phantom with water as the coupling medium, and the touching site was the same spot pointed to by the probe laser beam. The absolute acoustic pressure p_{abs} at the side surface of the phantom, as measured by the calibrated needle hydrophone, was 8100 Pa. The detection sensitivity of the heterodyne interferometer was quantified by the noise equivalent detectable pressure p_{NEP}, which was calculated by

$$p_{\text{NEP}}=\frac{\upsilon_{\text{noise}}}{\upsilon_{\text{signal}}}p_{\text{abs}}, \quad (12)$$

where v_{signal} and v_{noise} are the peak-to-valley (PV) amplitude of the signal and the root-mean-square (RMS) amplitude of the noise, respectively [17]. With v_{signal} = 18.7 mm/s and v_{noise} = 1.86 mm/s, p_{NEP} of the interferometer was quantified as 810 Pa for this case.

The detection bandwidth of the interferometer was also evaluated by comparing the Fourier spectrum of the signal measured by the interferometer with that from the calibrated needle hydrophone. The calibrated receiving frequency response is shown in III(c). As expected, the spectral profile is very flat in the designed detection band. The -6 dB bandwidth of the interferometer is approximately 1.2 MHz, which corresponds to a spatial resolution of 1.1 mm ($r_a = 0.88v/B$ for v = 1.54 mm/μs [2]) in PAI. As discussed later, the bandwidth and the sensitivity p_{NEP} of the interferometer are inversely proportional to each other. The narrow bandwidth used here is to ensure satisfactory sensitivity.

The measurement accuracy of the interferometer is subject to a variety of influences, such as laser wavelength instability, photodetector nonlinearity, and electronic processing noise. Among these, electronic processing noise is the most significant one. Thanks to the advances in digital Doppler signal demodulation, the accuracy of the heterodyne interferometer has been greatly improved compared with the ones using analog demodulation. The measurement error is typically less than 1% [41], which ensures the accuracy of the imaging results.

IV. Experimental Results

A. Non-Contact Boundary Delineation of Brain Tumor

Brain tumor is a kind of disease that involves cancerous or noncancerous growth of abnormal cells in the brain. For aggressive malignant brain tumors, surgical excision is usually inevitable [11]. Accurate demarcation of neoplastic tissue boundary is critical to the survival or health of the patients. Current practice used in brain tumor surgery still relies on tumor boundary identification by naked eyes, which can be misleading and risky due to the infiltrative nature of neoplastic tissues. Our previous work has shown that PAI can differentiate brain tumor from background tissue when the tumor is labelled with an optical contrast agent [11]. In comparison with florescence imaging which has been adapted to image-guided surgery of brain tumor, PAI, with good sectioning ability, is able to map a tumor in a three-dimensional manner, presenting not only the tumor boundaries in the horizontal plane, but also the tumor extension along the depth. Previous studies of PAI for guiding brain tumor surgery [11], [42], however, are all based on the use of piezoelectric transducers. To acquire an image, the probe needs to have a good contact with brain surface, which may turn out to be difficult to perform through a small-size access window in the skull. With the requirements of surface touching and applying of acoustic coupling material, the imaging procedure would inevitably interfere with the surgery. In this experiment, we want to explore the feasibility of brain tumor imaging and boundary delineation by using PAI with a non-contact design.

The experiment was performed on an *ex vivo* swine brain model. The whole head was harvested after the pig was euthanized. The scalp was removed and the top part of the skull was opened for brain exposure. A square gel block (width: 7.0 mm, thickness: 2.0 mm)

containing Coomassie Blue (CB) G-250 dye (20278, Sigma-Aldrich) was fabricated and embedded in the brain as an artificial tumor to mimic the situation of real brain tumor labelled with optically absorbing contrast agent [IV-B(a)]. The concentration of the CB dye in the gel block was 10 μg/mL (12 μM). The CB dye was adopted in the experiment because it is a common dye used to aid in brain tumor visualization, and 10 μg/mL is a typical concentration enabling the tumor to be recognized by naked eyes [11].

Figure 3 shows the experimental setup. The excitation laser working at 595 nm with a repetition rate of 10 Hz and pulse duration of 6 ns was from a dye laser (ND6000, Continuum Inc.), which was pumped by the second harmonic output of a Nd:YAG laser (Powerlite DLS 8010, Continuum Inc.). After passing through an iris, the laser beam was deflected by a mirror onto the surface of the pig brain. The size of the excitation laser beam on the brain surface was about 1.0 mm. The probe laser at 1550 nm from the interferometer was weakly focused onto the center of the excitation laser spot by an objective (focal length 250 mm, numerical aperture NA = 0.1, diffraction-limited laser spot diameter about 4.0 μm) to detect instantaneous surface vibration. To realize a B-scan, the sample (i.e., the pig head) was fixed on a linear translation stage, and moved horizontally at a step size of 250 μm. The laser, the interferometer, and the stage were synchronized by the trigger from the excitation laser. The measured signals were first decoded by the controller of the interferometer, and then digitized and recorded by an oscilloscope at a sampling rate of 50 MS/s (TDS 540, Tektronix Inc., Beaverton, OR). The laser fluence used in the experiment was estimated to be 24 mJ/cm^2.

Figure 4(b) presents a typical experimentally acquired B-scan image of the artificial tumor with 40 averages and its envelope after Hilbert transform. The red and the blue parts in the B-scan image represent the positive and the negative components of the PA signals from the tumor, and the black part of the image is background brain tissues. Apparently, the tumor is distinguishable from background tissues because of clearly delineated boundaries both in the horizontal plane (x-y) and along the depth direction (x-z). Specifically, in the horizontal plane, the boundaries are demarcated by noticeable signal amplitude differences between the tumor (red and blue parts) and background tissues (black part). Along the depth, the thickness of the tumor is determined by the time of flight (TOF) difference between phase-inverted signals (i.e., the positive signal and the negative signal) from the top and the bottom surfaces of the tumor. One typical A-line signal, shown in IV-B(c), was extracted from the B-scan image for closer study of the characteristics of the signals. There is a minor time lag between the negative signal and the positive signal, which indicates they are from the bottom and the top surfaces, respectively. The thickness of the tumor was in turn characterized to be about 1.9 mm using the measured TOF difference (1.26 μs), which is very close the actual thickness 2.0 mm. The processed B-scan image after Hilbert transform shows the volume of the tumor, as shown in IV-B(b). The experimental results reveal that, using the interferometer based non-contact PAI system, boundaries of brain tumors can be accurately profiled, which could provide reliable intraoperative guidance for brain tumor surgery in the future.

B. Non-Contact Photoacoustic Tomography

In this experiment, we sought to achieve tomographic PAI (i.e., photoacoustic tomography, or PAT) of biological samples by using the non-contact design.

Two cylindrical phantoms (50 mm for both diameter and thickness) were made from 10% gelatin solution mixed with Intralipid 20% (Fresenius Kabi, Uppsala, Sweden) with a volume ratio 1:1. The human tissue mimicking background (10% intralipid) has an absorption coefficient of 0.008 cm^{-1} and a reduced scattering coefficient of 152 cm^{-1} at 532 nm [43], [44]. In the first phantom [Fig. 5(a)], three black rubber disks (4 mm in diameter and 1 mm in thickness) were embedded in the phantom. In the second phantom [Fig. 5(c)], a piece of fat tissue (30 mm in diameter and 12 mm in thickness) was first embedded in the background gel, and then overlaid with two chicken gizzard cubes (5 mm in size) on the top. The top surfaces of both phantoms were covered with 3 mm thick background scattering gel. The inclusions in the final phantoms were invisible from the top with naked eyes.

Figure 6 shows the schematic of the interferometer based non-contact PAT system. The data acquisition was achieved using a circular scan geometry realized by a rotation stage. The excitation laser working at 532 nm was the second harmonic output of the same Nd:YAG laser. The outgoing laser beam was expanded in diameter by a concave lens to achieve uniform illumination of the samples, which were coaxially placed on a motorized rotation stage. The probe laser at 1550 nm from the interferometer was perpendicularly pointed at and weakly focused onto the side surface of the sample to detect surface vibration. The laser, the interferometer, and the stage were synchronized by the trigger from the excitation laser. The detected vibration signals were first demodulated by the controller of the interferometer, and then digitized and recorded by the oscilloscope. The excitation laser fluence used in the experiment was estimated to be 18 mJ/cm^2.

In the experiment, data were acquired over 120 rotation steps with an angular interval of 3°, covering the entire circle. Measured PA signals were averaged 300 times for each data acquisition step to enhance the SNR. The reconstructed images of the two phantoms using a back-projection algorithm [45] are shown in Figs. 5(b) and 5(d). Apparently, although not visible to naked eyes, the three black rubber disks, and the two chicken gizzard cubes were remarkably identifiable in the PAI images. The contrast-to-noise ratios (CNRs) of the black rubber image and the chicken gizzard image were quantified to be 15.6 dB and 6.0 dB, respectively.

V. Discussion

A. Acoustic Pressure, Particle Displacement and Particle Velocity

The three physical quantities, i.e., acoustic pressure, surface particle displacement and surface particle velocity, are essentially interrelated. In the brain tumor boundary delineation experiment, the measured maximum surface particle velocity was about 2.6 $mm \cdot s^{-1}$ [see Fig. 4(c)]. This value matches our estimation by calculating the initial PA pressure.

The optical density (OD) of the CB dye at a concentration of 10 mg/mL was measured to be 0.39 at 595 nm (OD = 0.39) for 1 cm optical path length. The equivalent optical absorption

coefficient μ_a = ln 10 × OD ≈ 0.9 cm^{-1}. The estimated laser fluence F used in the experiment was approximately 24 $mJ \cdot cm^{-2}$ (F = 24 $mJ \cdot cm^{-2}$). According to these assumptions, the specific optical absorption or energy density [46] is

$$A_e = \mu_a F \approx 21.6 \mathrm{mJ \cdot cm^{-3}} = 21.6 \times 10^3 \mathrm{Pa}. \quad (13)$$

The initial photoacoustic pressure is

$$p_0 = \Gamma(25^\circ \mathrm{C}) A_e \approx 2950 \mathrm{Pa}, \quad (14)$$

where the Grüneisen parameter Γ of soft tissue approximately equals 0.1368 at 25°C [46]. Assuming ultrasound center frequency f_u = 1 MHz (typical in the experiment), the maximum surface particle velocity and displacement are estimated to be

$$v_{max} = 2 \times \frac{p_0}{Z} \approx 3.9 \mathrm{mm \cdot s^{-1}}, \quad (15)$$

$$\delta_{max} = \frac{v_{max}}{2\pi f_u} = \frac{p_0}{\pi f_u Z} \approx 0.62 \mathrm{nm}, \quad (16)$$

where the acoustic impedance of soft tissue Z = 1.5 × 10^6 Pa · s · m^{-1} and the factor 2 in Eq. (15) is due to the free boundary conditions [34]. Two meaningful conclusions can be drawn from the results. First, the surface particle velocity and displacement in the experiment are typically of the order of mm · s^{-1} and sub-nanometer, respectively. Second, the estimated particle velocity 3.9 mm · s^{-1} is in good agreement with the experimental result 2.6 mm· s^{-1}.

B. Theoretical Limit of Detection Sensitivity

The sensitivity of the heterodyne interferometer is theoretically limited by the quantum noise of the detector [47]. The minimum detectable particle displacement is defined when the SNR is reduced to one, i.e., SNR = 1. According to the criterion, the minimum detectable particle displacement [47] is

$$\delta_{min} = \frac{1}{2\pi} \left(\frac{h}{\eta} \right)^{1/2} \left(\frac{c\lambda}{RP} \right)^{1/2} B^{1/2}, \quad (17)$$

where h = 6.6 × 10^{-34} J · s is the Planck constant, η is the quantum efficiency of the detector, c is the speed of light, λ is the wavelength of the laser, R is the reflectivity of the sample surface, P is the laser power, and B is the bandwidth of the ultrasound. Taking Eqs.

(17) and (2) into account, it is easy to find that the particle displacement δ is only ultrasound bandwidth related, while the particle velocity υ depends on both ultrasonic frequency f_u and bandwidth.

In extreme cases, for quantum efficiency η = 100%, surface reflectivity R = 100%, laser wavelength λ = 1550 nm, and laser power P = 10 mW, the bandwidth-dependent sensitivity limit is

$$\frac{\delta_{\min}}{B^{1/2}} \approx 8.8 \times 10^{-16}\mathrm{m} \cdot \mathrm{Hz}^{-1/2}. \quad (18)$$

For ultrasound center frequency f_u = 1 MHz and bandwidth B = 1.2 MHz (as in this case), the theoretically minimum detectable surface particle displacement, particle velocity, and acoustic pressure are

$$\delta_{\min}=8.8 \times 10^{-16}\mathrm{m} \cdot \mathrm{Hz}^{-1/2} \times B^{1/2} \approx 0.96\mathrm{pm}, \quad (19)$$

$$\upsilon_{\min}=2\pi f_u \delta_{\min} \approx 6.0\mu\mathrm{m} \cdot \mathrm{s}^{-1}, \quad (20)$$

$$p_{\min}=Z\upsilon/2 \approx 4.5\mathrm{Pa}. \quad (21)$$

The minimum detectable pressure (810 Pa) quantified in our experiment is about 200 times higher than the theoretical value (4.5 Pa).

C. Laser Safety

For the excitation laser, the laser fluence used in the brain tumor experiment was estimated to be 24 mJ · cm^{-2} at 595 nm, which is slightly higher than the maximum permissible exposure (MPE) of 20 mJ · cm^{-2} in the visible band according to the ANSI (American National Standards Institute) safety limit [48]. This value could be reduced to comply with the safety limit without seriously affecting the SNR. The laser fluence used in the PAT experiment was estimated to be 18 mJ · cm^{-2} at 532 nm, which is below the MPE and considered to be safe.

For the detection laser, the light source employed in the heterodyne interferometer is a 10 mW continuous wave (CW) laser working at 1550 nm. In the PAT experiment, for each rotation step with 300 signal averages (30 seconds exposure duration for 10 Hz repetition rate laser), the total amount of laser exposure is 2.0 ×10^4 W · cm^{-2} [$P/(\pi r^2)$, P = 10 mW, r = 0.51 λ/NA/2 = 4.0 μm is the radius of the laser spot on the sample surface for NA = 0.1 objective], which is about five orders of magnitude higher than the MPE of 0.1 W · cm^{-2} at

1550 nm according to the ANSI safety standard [48]. Although the detection laser was weakly focused onto the sample in the experiment, we here used the diffraction-limited laser spot size for fluence estimation to ensure laser safety in practical experiment. The safety issue could be solved by reducing the laser exposure time, which can be achieved by employing a pulsed probe laser or modulating the continuous probe laser into a pulsed one [32]–[34]. In this way, for single-shot measurements, the maximum permissible pulse duration of the probe laser is 50 μs [$(\pi r^2 \times \text{MPE})/P$, MPE = 1 J · cm^{-2} for exposure time below 10 seconds], which gives sufficient time for PA signal acquisition. In other words, as long as the laser pulse duration is less than 50 μs, the probe laser can be considered safe.

VI. Conclusion

In conclusion, we reported a study of achieving all-optical non-contact PAI by using a commercially available heterodyne interferometer working at 1550 nm. The interferometer remotely detects ultrasound-induced surface vibration without involving any physical contact with the sample. The theoretically predicated and experimentally measured noise equivalent detection limits of the interferometer were about 4.5 Pa and 810 Pa over 1.2 MHz bandwidth. The relationship between acoustic pressure, surface particle displacement and particle velocity were investigated. By using the interferometer, boundaries of an artificial tumor in a pig brain were accurately delineated, and biological samples in an optically scattering background were tomographically reconstructed, both in a non-contact manner. The experimental results and the analyses from this study suggest that the heterodyne interferometer offers a promising method to achieve non-contact PAI, which could be potentially used in biomedical imaging.

Acknowledgments

This work was supported by the National Institutes of Health under Grant R01AR060350 and Grant R01CA186769.

References

1. Wang X, Pang Y, Ku G, Xie X, Stoica G, Wang LV. Noninvasive laser-induced photoacoustic tomography for structural and functional *in vivo* imaging of the brain. Nat Biotechnol. 2003; 21(7): 803–806. [PubMed: 12808463]
2. Wang LV, Hu S. Photoacoustic tomography: In vivo imaging from organelles to organs. Science. 2012; 335(6075):1458–1462. [PubMed: 22442475]
3. Keswani RK, Tian C, Peryea T, Gandikota G, Wang X, Rosania GR. Repositioning clofazimine as a clinical macrophage-targeting photoacoustic contrast agent. Sci Rep. Mar.2016 6:23528. [Online]. Avilable: http://www.nature.com/articles/srep23528. [PubMed: 27000434]
4. Tian C, Xie Z, Fabiilli ML, Wang X. Imaging and sensing based on dual-pulse nonlinear photoacoustic contrast: A preliminary study on fatty liver. Opt Lett. 2015; 40(10):2253–2256. [PubMed: 26393712]
5. Tian C, et al. Dual-pulse nonlinear photoacoustic technique: A practical investigation. Biomed Opt Exp. 2015; 6(8):2923–2933.
6. Xu G, et al. High resolution physio-chemical tissue analysis: Towards non-invasive *in vivo* biopsy. Sci Rep. Feb.2016 6:16937. [PubMed: 26842459]
7. Feng T, et al. Bone assessment via thermal photo-acoustic measurements. Opt Lett. 2015; 40(8): 1721–1724. [PubMed: 25872057]

8. Deań-Ben XL, Pang GA, de Espinosa FM, Razansky D. Non-contact optoacoustic imaging with focused air-coupled transducers. Appl Phys Lett. 2015; 107(5):051105.
9. Tian, C., et al. Plasmonic nanoparticles with quantitatively controlled bioconjugation for photoacoustic imaging of live cancer cells; Adv Sci. Sep. 2016 p. 1600237[Online]. Avilable: http://onlinelibrary.wiley.com/doi/10.1002/advs.201600237/full
10. Paltauf G, Nuster R, Haltmeier M, Burgholzer P. Experimental evaluation of reconstruction algorithms for limited view photoacoustic tomography with line detectors. Inverse Probl. 2007; 23(6):s81.
11. Ray A, et al. Targeted blue nanoparticles as photoacoustic contrast agent for brain tumor delineation. Nano Res. 2011; 4(11):1163–1173.
12. Zhang HF, Maslov K, Stoica G, Wang LV. Imaging acute thermal burns by photoacoustic microscopy. J Biomed Opt. 2006; 11(5):054033. [PubMed: 17092182]
13. de La Zerda A, et al. Photoacoustic ocular imaging. Opt Lett. 2010; 35(3):270–272. [PubMed: 20125691]
14. Zhang E, Laufer J, Beard P. Backward-mode multiwavelength photoacoustic scanner using a planar Fabry-Perot polymer film ultrasound sensor for high-resolution three-dimensional imaging of biological tissues. Appl Opt. 2008; 47(4):561–577. [PubMed: 18239717]
15. Jathoul AP, et al. Deep *in vivo* photoacoustic imaging of mammalian tissues using a tyrosinase-based genetic reporter. Nature Photon. 2015; 9(4):239–246.
16. Ashkenazi S, Hou Y, Buma T, O'Donnell M. Optoacoustic imaging using thin polymer étalon. Appl Phys Lett. 2005; 86(13):134102.
17. Hou Y, Huang SW, Ashkenazi S, Witte R, O'Donnell M. Thin polymer etalon arrays for high-resolution photoacoustic imaging. J Biomed Opt. 2008; 13(6):064033. [PubMed: 19123679]
18. Chow CM, et al. Broadband optical ultrasound sensor with a unique open-cavity structure. J Biomed Opt. 2011; 16(1):017001. [PubMed: 21280922]
19. Peterson R, Solis S, Zhang B, Huang H, Ye JY. Sensitivity enhancement of an open-cavity-based optoacoustic sensor. Opt Lett. 2013; 38(15):2739–2741. [PubMed: 23903128]
20. Peterson RW, Kadugodinandareddy K, Karunakaran V, Whitney C, Ling J, Ye JY. Utilizing an open-microcavity optoacoustic sensor for spectroscopic determination of methemoglobin concentration. Proc SPIE. Mar.2015 9319:93191N.
21. Xie Z, Chen SL, Ling T, Guo LJ, Carson PL, Wang X. Pure optical photoacoustic microscopy. Opt Exp. 2011; 19(10):9027–9034.
22. Xie Z, et al. 3D high resolution photoacoustic imaging based on pure optical photoacoustic microscopy with microring resonator. Proc SPIE. Mar.2014 8943:894314.
23. Zhang C, Chen SL, Ling T, Guo LJ. Review of imprinted polymer microrings as ultrasound detectors: Design, fabrication, and characterization. IEEE Sens J. Jun; 2015 15(6):3241–3248.
24. Chen SL, Guo LJ, Wang X. All-optical photoacoustic microscopy. Photoacoustics. 2015; 3(4):143–150.
25. Li H, Dong B, Zhang Z, Zhang HF, Sun C. A transparent broadband ultrasonic detector based on an optical micro-ring resonator for photoacoustic microscopy. Sci Rep. Mar.2014 4:4496. [PubMed: 24675547]
26. Dong B, Chen S, Zhang Z, Sun C, Zhang HF. Photoacoustic probe using a microring resonator ultrasonic sensor for endoscopic applications. Opt Lett. 2014; 39(15):4372–4375. [PubMed: 25078180]
27. Rosenthal A, Razansky D, Ntziachristos V. High-sensitivity compact ultrasonic detector based on a pi-phase-shifted fiber Bragg grating. Opt Lett. 2011; 36(10):1833–1835. [PubMed: 21593906]
28. Maswadi, SM., et al. All-optical optoacoustic microscopy based on probe beam deflection technique. Photoacoustics. Feb. 2016 [Online]. Available: http://www.sciencedirect.com/science/article/pii/S2213597916300076
29. Nuster R, Slezak P, Paltauf G. High resolution three-dimensional photoacoustic tomography with CCD-camera based ultrasound detection. Biomed Opt Exp. 2014; 5(8):2635–2647.
30. Speirs RW, Bishop AI. Photoacoustic tomography using a Michelson interferometer with quadrature phase detection. Appl Phys Lett. 2013; 103(5):053501.

31. Carp SA, Venugopalan V. Optoacoustic imaging based on the interferometric measurement of surface displacement. J Biomed Opt. 2007; 12(6):064001. [PubMed: 18163817]
32. Hochreiner A, Bauer-Marschallinger J, Burgholzer P, Jakoby B, Berer T. Non-contact photoacoustic imaging using a fiber based interferometer with optical amplification. Biomed Opt Exp. 2013; 4(11):2322–2331.
33. Hochreiner A, Berer T, Grün H, Leitner M, Burgholzer P. Photoacoustic imaging using an adaptive interferometer with a photorefractive crystal. J Biophotonics. 2012; 5(7):508–517. [PubMed: 22354686]
34. Rousseau G, Blouin A, Monchalin JP. Non-contact photoacoustic tomography and ultrasonography for tissue imaging. Biomed Opt Exp. 2012; 3(1):16–25.
35. Rousseau G, Gauthier B, Blouin A, Monchalin JP. Non-contact biomedical photoacoustic and ultrasound imaging. J Biomed Opt. 2012; 17(6):061217. [PubMed: 22734747]
36. Wang Y, Li C, Wang RK. Noncontact photoacoustic imaging achieved by using a low-coherence interferometer as the acoustic detector. Opt Lett. 2011; 36(20):3975–3977. [PubMed: 22002357]
37. Blatter C, et al. Intrasweep phase-sensitive optical coherence tomography for noncontact optical photoacoustic imaging. Opt Lett. 2012; 37(21):4368–4370. [PubMed: 23114298]
38. Chen Z, Yang S, Wang Y, Xing D. Noncontact broadband all-optical photoacoustic microscopy based on a low-coherence interferometer. Appl Phys Lett. 2015; 106(4):043701.
39. Horstmann J, Spahr H, Buj C, Münter M, Brinkmann R. Full-field speckle interferometry for non-contact photoacoustic tomography. Phys Med Biol. 2015; 60(10):4045. [PubMed: 25927910]
40. Dräbenstedt A, Sauer J, Rembe C. Remote-sensing vibrometry at 1550 nm wavelength. Proc 10th Int Conf Vibrat Measurements Laser Noncontact Techn-AIVELA (AIP). 2012:113–121.
41. Lawrence EM, Rembe C, Boedecker S, Zhang H. The ultra fine dynamics of MEMS as revealed by the Polytec micro system analyzer. Proc SPIE. Jan.2006 6111:61110L.
42. Kircher MF, et al. A brain tumor molecular imaging strategy using a new triple-modality MRI-photoacoustic-Raman nanoparticle. Nat Med. 2012; 18(5):829–834. [PubMed: 22504484]
43. Van Staveren HJ, Moes CJ, van Marie J, Prahl SA, Van Gemert MJ. Light scattering in lntralipid-10% in the wavelength range of 400–1100 nm. Appl Opt. 1991; 30(31):4507–4514. [PubMed: 20717241]
44. Flock ST, Jacques SL, Wilson BC, Star WM, van Gemert MJ. Optical properties of Intralipid: A phantom medium for light propagation studies. Lasers Surg Med. 1992; 12(5):510–519. [PubMed: 1406004]
45. Xu M, Wang LV. Universal back-projection algorithm for photoacoustic computed tomography. Phys Rev E. 2005; 71(1):016706.
46. Wang, LV., Wu, HI. Biomedical Optics: Principles and Imaging. Hoboken, NJ, USA: Wiley; 2012.
47. Dewhurst RJ, Shan Q. Optical remote measurement of ultrasound. Meas Sci Technol. 1999; 10(11):R139.
48. American National Standard for Safe Use of Lasers. Laser Institute of America, Amer. Nat. Standards Institute, Inc; 2007. ANSI Standard Z136.1-2007

Biographies

Chao Tian (M′14) received the B.S. degree in electrical engineering and the Ph.D. degree in optical engineering from Zhejiang University, Hangzhou, China, in 2008 and 2013, respectively. Since 2013, he has been a Post-Doctoral Research Fellow with the University of Michigan, Ann Arbor. He has authored over 30 peer-reviewed journal papers and six inventions. His research interests include optical imaging, optical sensors, and optical testing.

Ting Feng received the B.S. and M.S. degrees in electrical engineering from Nanjing University, Nanjing, China, in 2010 and 2012, respectively, where she is currently pursuing

the Ph.D. degree. She is a Visiting Ph.D. student with the University of Michigan, Ann Arbor. Her research interests include photoacoustic imaging and computer vision.

Cheng Wang received the B.S. degree in physics from Inner Mongolian Normal University, Huhehaote, China, in 1999, and the M.S. and Ph.D. degrees in optics from the Changchun Institute of Optics and Fine Mechanics and Physics, Changchun, China, in 2002 and 2005, respectively. He was a Post-Doctoral Researcher with Shanghai Jiaotong University, Shanghai, China, from 2005 to 2007. He is currently an Associate Professor with the University of Shanghai for Science and Technology, Shanghai, China. His research interests include the development of biological/medical imaging and treatment techniques.

Shengchun Liu received the M.S. degree in electronic engineering from Heilongjiang University, Harbin, China, in 2005, and the Ph.D. degree in fiber technology from Nanjing University, Nanjing, China, in 2011. He is currently a Professor with Heilongjiang University, Harbin, China. He has authored one book, more than 50 articles and more than 15 inventions. His research interests include optical sensors, fiber laser, DBF laser, and photoacoustic detection.

Qian Cheng received the B.S. degree in physics, and the M.S. and Ph.D. degrees in acoustics from Tongji University, Shanghai, China, in 2000, 2003, and 2006, respectively. She was a Lecturer with Tongji University from 2006 to 2009. She is currently an Associate Professor with Tongji University. Her research interest includes the development of biological/medical imaging and treatment techniques using ultrasound and photoacoustics, atomic force acoustic microscopy, near field scanning photoacoustic microscopy, industry NDT, and fiber acoustic sensor.

David E. Oliver received the degree (Hons.) in physics with astrophysics from the University of Leicester, U.K. in 1977. He was with the Design and Development of Sophisticated Optical Measurement Systems, SIRA (formerly the British Scientific Instrument Research Association), before working in applications development and then sales and marketing. He has over 30 years of experience in laser Doppler vibrometry and is credited with introducing scanning laser Doppler vibrometry into commercialization during the mid-eighties. He is currently Chief Technology Officer and the VP of Business Development.

Xueding Wang received the B.S. degree in electronic engineering and the M.S. degree in acoustics from Nanjing University, Nanjing, China, in 1997 and 2007, respectively, and the Ph.D. degree in biomedical engineering from Texas A&M University, College Station, TX, USA. He is currently an Associate Professor with the Department of Biomedical Engineering, University of Michigan, holding an Adjunct Associate Professor position at the Department of Radiology.

Guan Xu received the B.S. degree in electrical engineering from the Hebei University of Technology, Tianjin, China, in 2006, and the Ph.D. degree in electrical engineering from Oklahoma State University, Stillwater, OK, USA, in 2011. He joined the Department of Radiology, University of Michigan, as a Post-Doctoral Research Fellow, in 2012. He has

been a Research Investigator with the University of Michigan since 2014. His research interest includes biomedical optics technologies and their clinical applications.

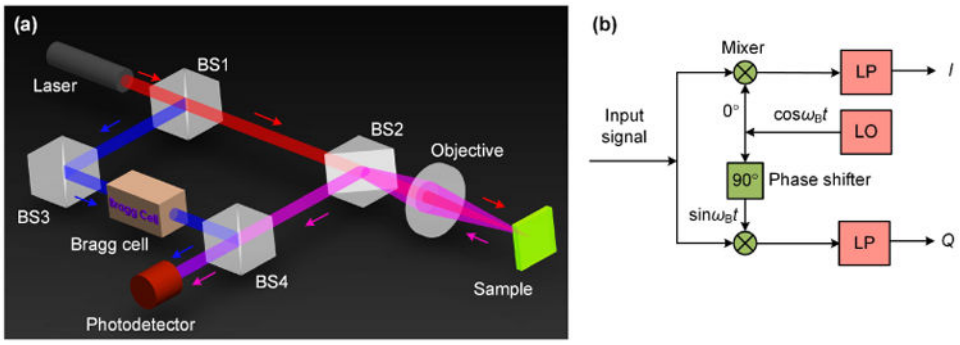

Fig. 1.

Schematic of the heterodyne interferometer (a), and in-phase and quadrature (IQ) demodulation (b). BS: beam splitter, LO: local oscillator, LP: low-pass filtering.

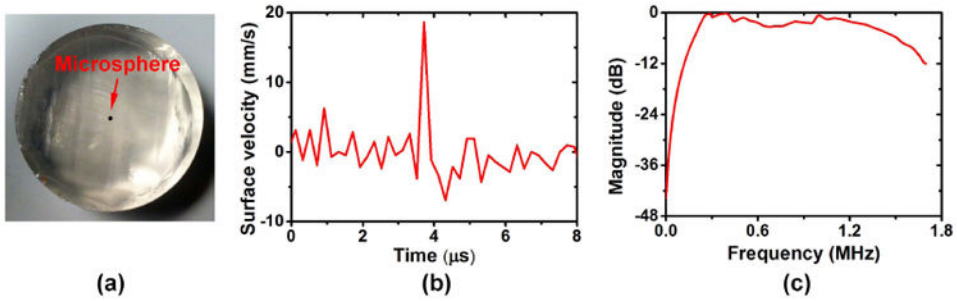

Fig. 2.

Performance characterization of the heterodyne interferometer. (a) Photogram of a gel phantom containing a 500-μm diameter microsphere as a point target. (b) Received PA signal from the point object. (c) Calibrated receiving frequency response.

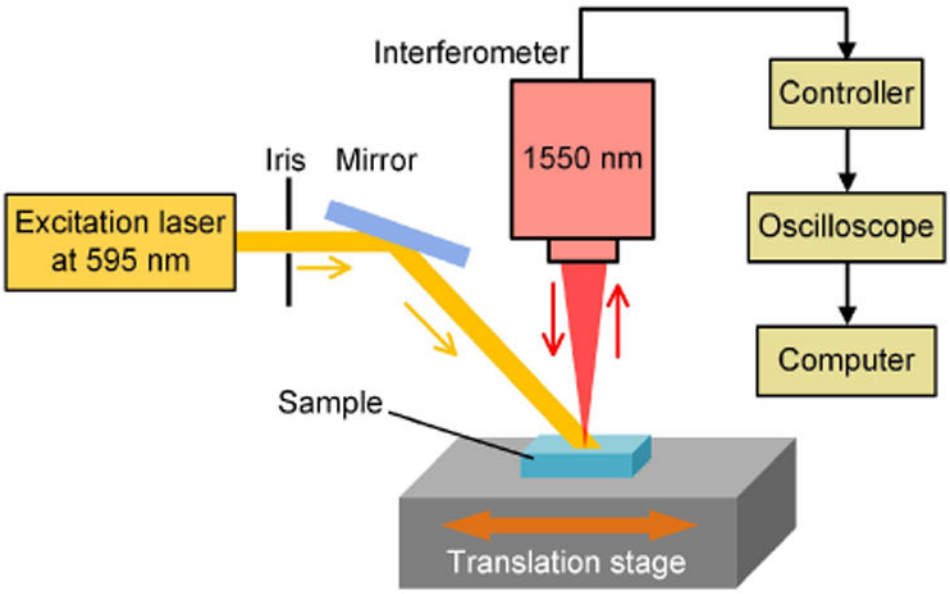

Fig. 3.
Schematic of non-contact PAI of brain tumor.

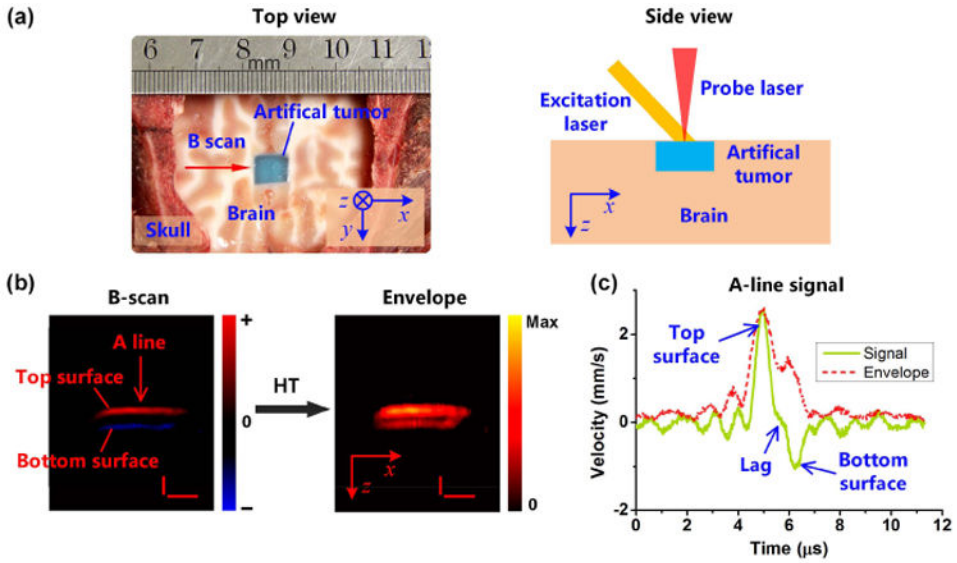

Fig. 4.

Non-contact boundary delineation of an artificial brain tumor. (a) A top-view photograph showing the exposed pig brain with the tumor (i.e., a gel block) embedded. A side-view sketch showing the plane for the B-scan which was performed by a raster scan across the tumor. (b) (left) A B-scan image of the brain tumor acquired in a non-contact manner. Red and blue parts show positive and negative components of the measured velocity. (right) The processed image after Hilbert transform (HT), where the volume of the tumor can be recognized clearly. (c) One typical A-line signal of the tumor and its envelope. Horizontal and vertical bars: 2 mm.

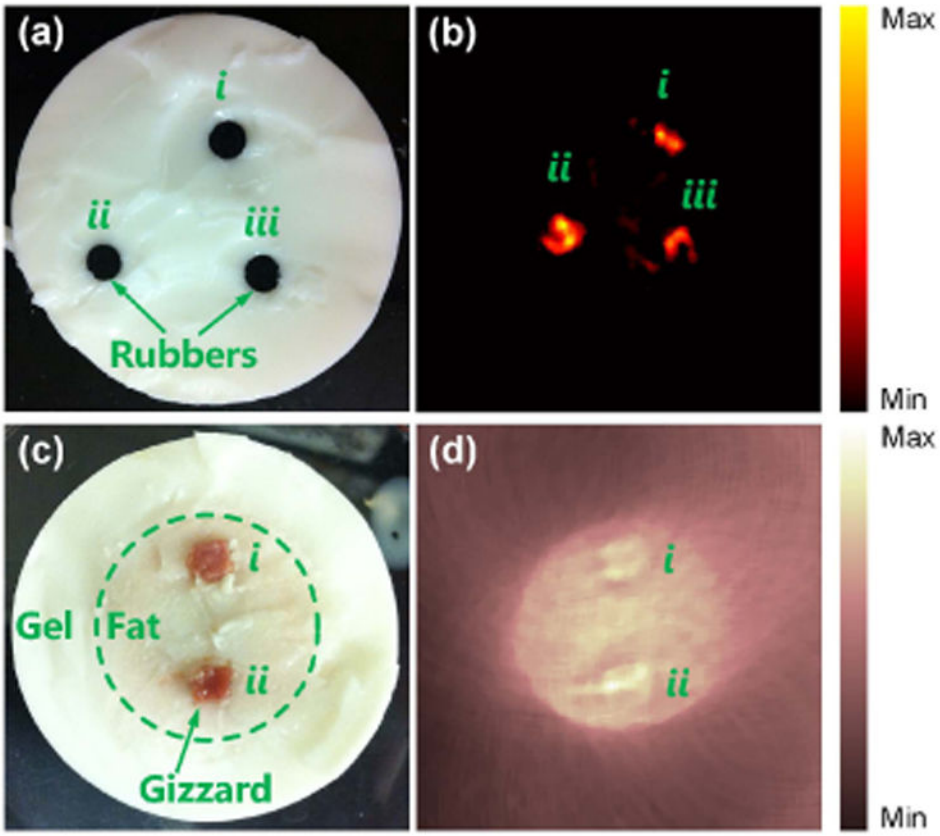

Fig. 5.

Phantoms and imaging results: (a) and (b) cross section and reconstructed image of the phantom with black rubber inclusions and (c) and (d) cross section and reconstructed image of the phantom with the fat tissue (in the dashed circle) and the chicken gizzards. In the experiment, the phantoms were covered with 3 mm thick optical scattering layers with 10% intralipid.

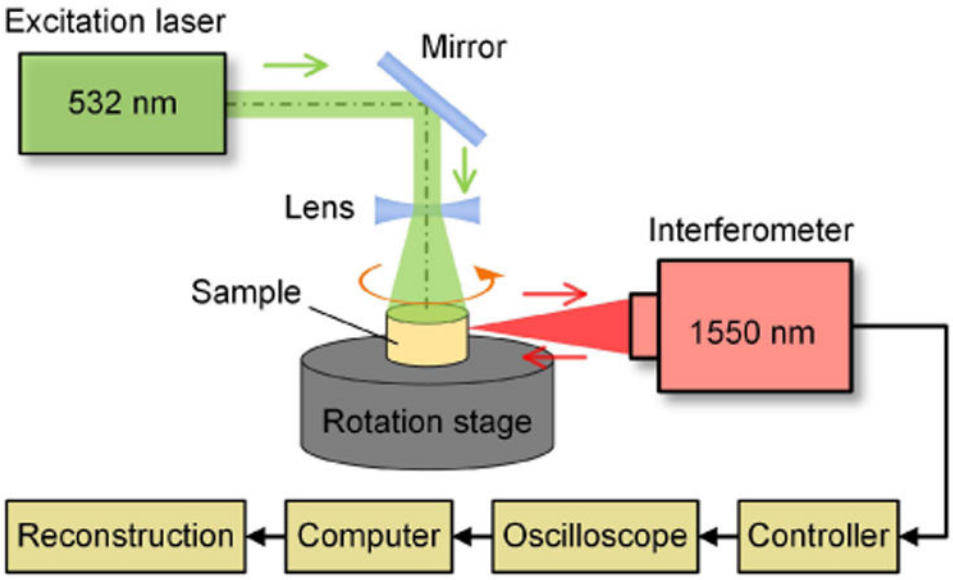

Fig. 6.
Schematic layout of the non-contact PAT.